The Astrophysical Journal, 872:4 (16pp), 2019 February 10 https://doi.org/10.3847/1538-4357/aafcb2

Particle Acceleration at 5 au Associated with Turbulence and Small-scale Magnetic Flux Ropes

L.-L. Zhao[1], G. P. Zank[1,2,3], Y. Chen[2], Q. Hu[1,2], J. A. le Roux[1,2], S. Du[2], and L. Adhikari[1]
[1] Center for Space Plasma and Aeronomic Research (CSPAR), University of Alabama in Huntsville, Huntsville, AL 35805, USA
[2] Department of Space Science, University of Alabama in Huntsville, Huntsville, AL 35899, USA
Received 2018 October 9; revised 2019 January 4; accepted 2019 January 7; published 2019 February 6

Abstract

An observational analysis of an atypical energetic particle event near 5 au measured by the *Ulysses* spacecraft is presented. A previous study has attributed the unusual enhancement of energetic proton flux to the presence of small-scale dynamic magnetic islands or flux ropes. Here, we find that the generation of these magnetic islands may be related to the interaction of a stream interaction region (SIR) and the heliospheric current sheet (HCS). Particles are accelerated and trapped within the SIR structure characterized by a forward shock–reverse wave pair. Analysis of the energetic particle intensity spectra shows that the 63 keV–4.4 MeV protons form a power-law (PL) spectrum near the shock, with a slope much steeper than predicted by the diffusive shock acceleration (DSA) theory. Double PL spectra are found in the region of unusual particle flux enhancement, and the lower energy part of the spectrum gets harder farther away from the shock. In comparison, we discuss a later forward wave–reverse wave pair with an embedded large-scale magnetic cloud (MC). In contrast to small-scale magnetic islands, the MC corresponds to a decrease in energetic proton fluxes. A power spectral density analysis suggests that the turbulence level increases in the compression regions, and the majority of the observed turbulence power resides in the two-dimensional (2D) component because the spacecraft velocity is almost perpendicular to the interplanetary magnetic field. This is consistent with the enhanced generation of magnetic flux ropes, which are instrinsic to quasi-2D MHD turbulence, in the SIR. An automatic Grad–Shafranov reconstruction technique is used to identify flux rope structures within the period of interest, and their detailed parameters are included in the paper. The observational evidence suggests that the interaction of shock/compressional waves with the HCS may be a key element in generating small-scale dynamic magnetic islands, which subsequently accelerate charged particles and complement the classical DSA mechanism.

Key words: acceleration of particles – magnetic reconnection – shock waves – solar wind

1. Introduction

A recent study of *Ulysses* measurements (Zhao et al. 2018b) suggests that an unusual energetic particle flux enhancement downstream of an interplanetary shock (IS) near 5 au may be related to small-scale magnetic flux rope (or island/plasmoid) dynamics. Zhao et al. showed that the extended Zank et al. (2014) transport theory of stochastic particle acceleration via magnetic reconnection processes accounts successfully for the observed energetic particle "time–intensity" profile and spectra downstream of the shock. Observational evidence and modeling of local magnetic flux rope structures using *Ulysses* solar wind plasma and magnetic field data on the basis of the Grad–Shafranov (GS) reconstruction technique (Sonnerup & Guo 1996; Hau & Sonnerup 1999; Hu et al. 2004; Hu 2017) are also reported in Zhao et al. (2018b) and Chen et al. (2018). Here we investigate in detail the event presented in Zhao et al. (2018b), analyzing the overall structure and properties of the event, including further discussion about the particle energization.

Magnetic flux ropes can be defined by a magnetic field configuration corresponding to helical field lines winding around a central axis. Small-scale magnetic flux ropes in the solar wind between 0.3 and 5.5 au have been identified and studied by using the *Helios* 1 and 2, *IMP* 8, *Wind*, *ACE*, *STEREO*, and *Ulysses* spacecraft measurements. For example, Yu et al. (2014, 2016) presented a comprehensive statistical analysis of small-scale flux ropes from 1995 to 2014 using *Wind* and *STEREO* data. A small-scale flux rope (e.g., a magnetic island) commonly has a duration from a few minutes up to a few hours with a scale size less than 0.01 at 1 au (Zheng & Hu 2018), while large-scale interplanetary magnetic flux ropes, such as magnetic clouds (MCs) associated with interplanetary coronal mass ejections (ICMEs), usually have an average duration of 21 hr, ranging from 8 to 48 hr at 1 au (Cartwright & Moldwin 2010). Large-scale flux rope structures or MCs have been investigated for decades and are generally characterized by (1) a smooth magnetic field rotation through a large angle, (2) enhanced magnetic field strength compared to the ambient solar wind, and (3) abnormally low proton temperature and low plasma beta (Burlaga et al. 1981; Ebert et al. 2009; Cartwright & Moldwin 2010). Unlike MCs that emerged from the Sun, the formation mechanism and origination of small-scale magnetic islands are still under investigation. Numerical simulations of decaying solar wind turbulence suggest that magnetic islands are coherent quasi-2D nonlinear structures generated from fully developed turbulence (Dmitruk et al. 2004; Greco et al. 2009; Servidio et al. 2009, 2010), which contains a dominant 2D component (Zank & Matthaeus 1992, 1993; Bieber et al. 1996; Matthaeus et al. 2007; Zank et al. 2017). In general, magnetic islands in the supersonic solar wind separated by discontinuities or current sheets (CSs) can originate from magnetic reconnection, MHD turbulence, and numerous instabilities (Chian & Muñoz 2011; Khabarova et al. 2015).

[3] Author of correspondence.

Magnetic reconnection in the solar wind can occur at CSs of various scales (Khabarova & Zank 2017). As a fundamental physical process related to energy conservation, magnetic reconnection has been widely invoked to explain the energization and heating of space plasma through the conversion of magnetic energy into plasma kinetic energy (e.g., Lu et al. 2013; Wang et al. 2016). A statistical acceleration mechanism for charged particles related to magnetic reconnection was first proposed by Matthaeus et al. (1984), Goldstein et al. (1986), and Ambrosiano et al. (1988), based on test-particle simulations. They found that turbulent fluctuations appearing in reconnection regions can trap test particles in the strong electric field for a sufficiently long time to produce significant acceleration. Based on these earlier ideas, several numerical simulations for particle acceleration via turbulent magnetic reconnection associated with multiple interacting magnetic islands have emerged (e.g., Drake et al. 2006; Oka et al. 2010; Le et al. 2012; Guo et al. 2014, 2015; Du et al. 2018; Lu et al. 2018). Simultaneous with these simulation developments, comprehensive transport theories for charged particles traversing numerous contracting and merging small-scale magnetic islands have been proposed by Zank et al. (2014, 2015) and further developed by le Roux et al. (2015, 2016, 2018). Reconnection associated with merging and contracting magnetic islands can yield a first-order Fermi process for the direct energization of particles trapped in the islands and also can be combined with other acceleration mechanisms, such as diffusive shock acceleration (DSA), to further accelerate trapped particles (Zank et al. 2015; le Roux et al. 2016). The theoretical solutions that can be derived from Zank et al. (2014, 2015) and le Roux et al. (2015, 2016, 2018) yield a power-law (PL)-like spectrum for the particle distribution.

The DSA mechanism is usually considered to be responsible for energizing charged particles at shock waves and provides an explanation for abundant gradual solar energetic particle events (Reames 1999; Zank et al. 2000, 2007; Li et al. 2003; Rice et al. 2003; Verkhoglyadova et al. 2015). As a classical mechanism for particle acceleration (Axford et al. 1977; Krymskii 1977; Bell 1978; Blandford & Ostriker 1978), DSA, in 1D stationary cases, predicts that the particle intensity peaks at the shock, after which it is a constant. The distribution of diffusively accelerated particles at and downstream of the shock is a PL with an index depending only on the shock compression ratio (Verkhoglyadova et al. 2015; Zank et al. 2015). However, steady-state DSA predictions do not always describe observations. In more realistic situations, the downstream particle intensities are often observed to decrease strongly (Neugebauer et al. 2006; Tessein et al. 2015). This may be due to enhanced adiabatic deceleration in the downstream (Kartavykh et al. 2016) or post-shock magnetic field structures. Atypical energetic particle events with energization up to MeV energies behind shock waves have been frequently observed both at 1 au (Tessein et al. 2013, 2015; Khabarova et al. 2015, 2016; Khabarova & Zank 2017) and in the outer heliosphere (Zank et al. 2015; Zhao et al. 2018b). They generally possess harder PL spectra than DSA predicts. The DSA mechanism relies on magnetic turbulence to scatter particles back and forth across the shock, but the contribution of the turbulence to the direct energization of particles may be underestimated. MHD turbulence downstream of the shock dissipates via highly dynamical localized reconnection events, generating magnetic islands, which can further energize charged particles through local stochastic processes.

Observational evidence suggests that the heliospheric current sheet (HCS) generates and confines small-scale flux ropes when disturbed. Due to the variability of the solar wind, magnetic reconnection occurs recurrently at the HCS (Gosling et al. 2006), resulting in effective magnetic island merging in the vicinity of the HCS. When the HCS interacts with ISs, corotating interaction regions (CIRs), and ICMEs, magnetic island merging and contracting are likely to be more efficient because of the increased reconnection rate and strong compression (Khabarova et al. 2015, 2016). This provides a possible explanation for the observed strong enhancements in particle flux behind shock waves, at the leading edge of ICMEs, as well as within CIRs. Compared to small-scale magnetic islands, which can accelerate charged particles stochastically, large-scale MCs that are associated with ICMEs often lead to a decrease in the energetic particle intensity. This can be understood as the strong MC field suppressing the entrance of energetic particles into the large-scale structures (Cane & Lario 2006).

In this paper, we present a detailed observational study of the unusual energetic particle event reported in Zhao et al. (2018b). As already shown by Zhao et al. (2018b), the Zank et al. (2014) theory quantitatively reproduces the energetic particle flux enhancement behind an IS and the evolution of the energetic particle spectrum. However, Zhao et al. (2018b) did not address what the conditions are that lead to such particle acceleration processes by magnetic islands. This is a key question that we investigate in this paper. The organization of this paper is as follows: Section 2 presents an overview of the *Ulysses* observations in a selected interval that lasted for 19 days. Section 3 shows the evolution of the energetic particle spectrum. Section 4 presents a power spectral density (PSD) analysis of our selected interval, which provides information on the turbulence properties. Section 5 illustrates the GS reconstruction technique and the reconstructed magnetic flux rope structures. The last section provides a summary and conclusions.

2. Overview of the Observations

Figure 1 displays a 19 day plot of an atypical energetic particle flux variation event associated with magnetic flux ropes during the period between 2004 February 13, 00:00 UT, and 2004 March 3, 00:00 UT, identified by Zhao et al. (2018b). The top panel shows the energetic ion count rates with hourly resolution measured by the *Ulysses* LEMS30 detector in eight energy channels: 56–78, 78–130, 130–214, 214–337, 337–594, 594–1073, 1073–1802, and 1802–4752 keV. The following panels show, respectively, the interplanetary magnetic field (IMF) strength $|B|$ with 1 minute resolution, the elevation (θ) and azimuthal (ϕ) angles of the magnetic field direction in the RTN coordinate system, the color-coded pitch angle distribution (PAD) of 116 eV suprathermal electrons from the *Ulysses* SWOOPS electron instrument, the ratio of proton thermal pressure to magnetic pressure (β_p), the 4–8 minute averaged proton density (n_p), proton temperature (T_p), flow speed (V), and the total pressure $P = 2n_p k_B T_p + B^2/2\mu_0$, where k_B is the Boltzmann constant and μ_0 is the magnetic permeability. Note that the measurements of electron PAD data, at a cadence of 7–34 minutes, are only available for six days (February 14–16 and February 25–27) during the period of interest. The particle

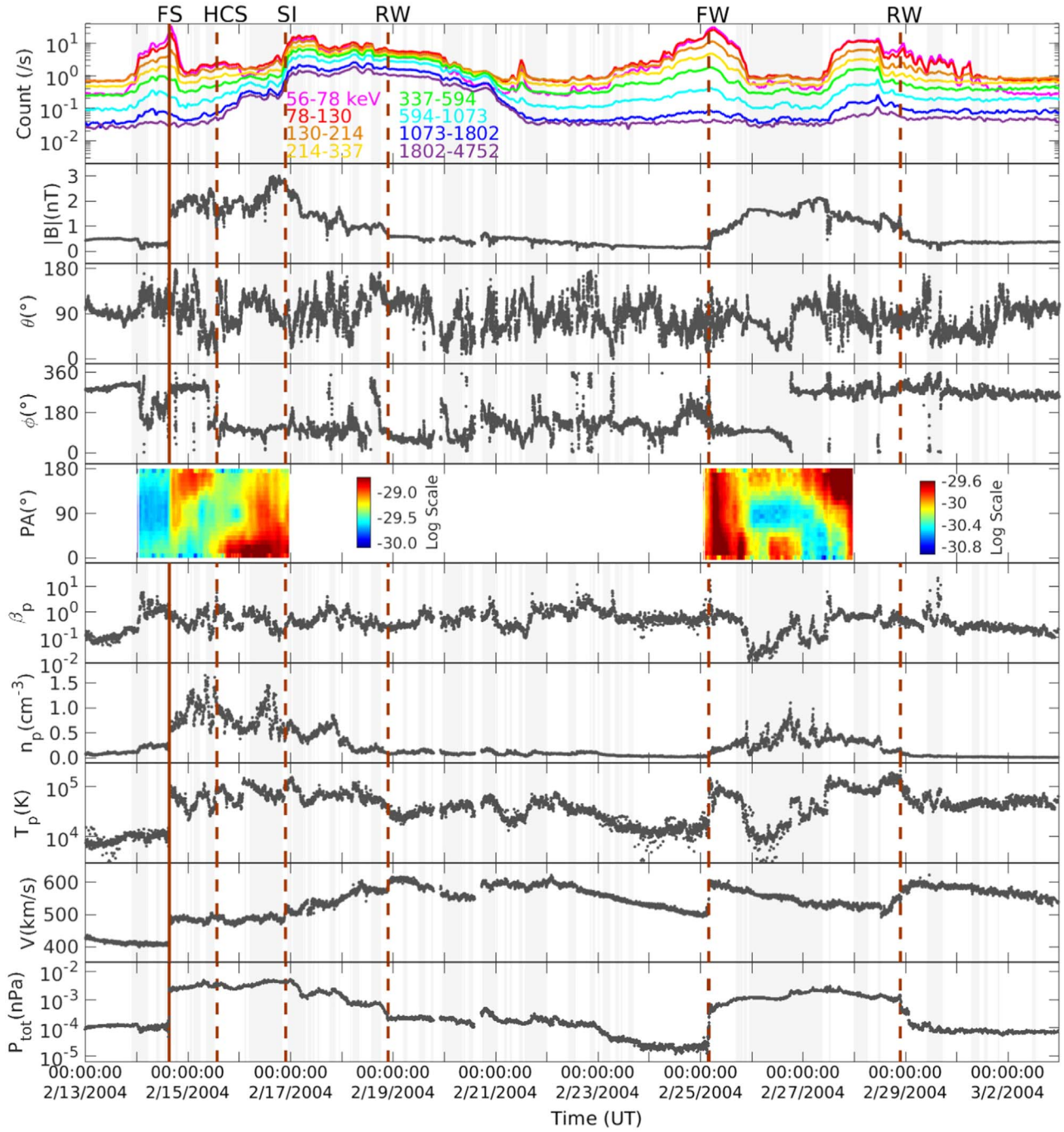

Figure 1. *Ulysses* in situ observations from 2004 February 13 to March 3. From top to bottom, the panels are the energetic ion counts for the eight energy channels listed, the magnetic field strength ($|B|$), the elevation (θ) and azimuthal (ϕ) angles of the magnetic field direction in the RTN coordinate system, the pitch angle distribution of 116 eV electrons, proton beta (β_p), proton density (n_p), proton temperature (T_p), solar wind speed (V), and the total plasma pressure ($P_{\rm tot}$). The vertical maroon line shows the observation time of the forward shock (FS). The dashed vertical lines behind the shock identify the location of the heliospheric current sheet (HCS), the stream interface (SI), the first reverse wave (RW), the forward wave (FW), and the second reverse wave (RW), respectively. Shaded areas are the GS reconstructed magnetic flux ropes.

counts, proton beta, temperature, and total pressure are plotted in log scale. Using the GS reconstruction technique, we identify 52 magnetic flux rope structures marked as shaded areas in the figure. We discuss these reconstructed flux rope structures in detail in Section 5.

During this period, *Ulysses* crossed the heliographic equator at ∼5.36 au. An IS swept over *Ulysses* at 15:15:27 UT on 2004 February 14 (http://ipshocks.fi/database), which was a forward shock (FS) characterized by abrupt increases in the IMF strength, proton density, velocity, temperature, and plasma pressure. There is a period of ∼15 hr preceding the FS, during which the energetic particle flux increases until the shock passage. The sudden increase in energetic particle flux (at ∼00:00 UT on February 14) indicates the presence of a local trapping boundary with very low IMF magnitude (close to 0) and high plasma beta (Trenchi et al. 2013; Tessein et al. 2016). The IMF also changes direction in this period. These observed signatures are consistent with a strong CS. However, due to the

lack of electron PAD observation for 2004 February 13, we cannot determine unambiguously whether it is connected to the HCS. At a later time behind the shock, an HCS crossing near 13:26 UT on February 15 was identified by sharp changes in the IMF direction. The HCS was a bifurcated CS associated with a directional change of the magnetic field as shown in the IMF elevation θ and azimuthal ϕ panels. Simultaneously, the IMF magnitude $|B|$ decreases, and the proton density n_p and temperature T_p increase at the HCS crossing, leading to a sharp increase in proton beta β_p ($\sim$10). In the electron PAD panel, there is a clear signature associated with the abrupt change in direction of the magnetic field, the unidirectional beam initially aligned with the 180° pitch angle before the HCS crossing, then the beam with a slightly larger intensity switched to 0° pitch angle after the HCS crossing. Previous studies suggest that the interaction of a shock and the HCS may create favorable downstream conditions for plasmoid-related particle acceleration, such as the production and confinement of magnetic flux ropes. After crossing the HCS, the energetic particle intensities begin to increase, especially for the higher energy particles (>337 keV) that were less accelerated near the shock front. Rather remarkably, Zhao et al. (2018b) chose the particle injection point to be near the HCS and successfully reproduced the observed energetic particle "time–intensity" profile and spectra downstream using a theory of stochastic acceleration by interacting magnetic islands. Here, we do not address the theoretical predictions again but focus exclusively on the explanation of the properties of plasmas and fields.

During the period from February 17, 00:00 UT, to February 19, 00:00 UT, the flow velocity V shows a slight and gradual increase from $\sim$500 to $\sim$600 km s^{-1}. The proton density n_p correspondingly shows an overall decrease, and the IMF magnitude $|B|$ also drops from $\sim$2 to $\sim$0.6 nT. There is no clear change in solar wind temperature T_p. These characteristics lead to a gradual decrease in total pressure by an order of magnitude. Remarkably, energetic particle intensities in this period exhibit a noticeable increase for all considered energy channels. Using the abnormally low proton temperature as the primary criterion, Du et al. (2010) identified one ICME starting at February 18, 23:02 UT, with a duration of 12 hr. However, this ICME is excluded from the *Ulysses* ICME catalog compiled by Ebert et al. (2009) and Richardson (2014), who used multiple solar wind signatures to identify ICMEs, probably because of the very low magnetic field strength ($\sim$0.6 nT) in the corresponding period. We notice that there may be a reverse wave near February 19, 0:00 UT, characterized by a moderate increase in proton velocity and decreases in density, temperature, and magnetic field strength. This suggests that the period from $\sim$February 14, 15:15 UT, to $\sim$February 19, 00:00 UT, may correspond to a stream interaction region (SIR) with a forward shock–reverse wave (FS–RW) pair, in which the HCS is embedded. The whole picture of this SIR structure is very similar to the interaction region observed by *Ulysses* in 1992 November at 5 au shown in Forsyth & Gosling (2001; Richardson 2018). The stream interface (SI) that separates the slow and fast solar wind is typically characterized by a transition that includes increasing flow speed and proton temperature, and decreasing plasma density. It is also indicated by a deflection in the transverse solar wind flow (Richardson 2018). There is no traditionally defined SI at *Ulysses* because the variations in plasma density and temperature are more gradual (Jian et al. 2009). Specifically, Wimmer-Schweingruber et al. (1997) reported that the interface may be crossed multiple times by *Ulysses* in some SIRs. The SI at 1 au has been defined by the peak of the total perpendicular pressure (Jian et al. 2009) or the peak of the proton density (Richardson 2018). Here, we plot the various observed parameters near the SIR in Figure 2. The six panels show, from top to bottom, the magnetic field magnitude $|B|$ and the components B_R, B_T, and B_N; solar wind speed V_S; transverse solar wind velocity components V_T and V_N; proton number density N_p; proton temperature T_p; and thermal, magnetic, and total pressures. The locations of FS, HCS, SI, and RW are labeled by vertical dashed lines. It shows the SI near 00:00 UT, February 17, indicated by a slight increase in flow velocity and a fall in proton density, IMF intensity, and total pressure. This interface is also indicated by a deflection in the transverse solar wind flow in T and N directions. The reverse wave near February 19, 00:00 UT, appears to coincide with decreasing energetic particle fluxes. The evidence presented here suggests that the compression due to the SIR together with the HCS crossing provide favorable conditions for particle energization and trapping in a bounded domain filled with small-scale flux rope structures.

During the period February 19, 00:00 UT, to February 22, 00:00 UT, *Ulysses* experienced a high-speed stream with low magnetic fluctuation levels. The proton density and temperature are comparatively low. Energetic particle intensities gradually decrease to quiet levels. At $\sim$10:00 UT on February 21, the lower energy particle fluxes show a spike-like structure. We note that the structure may be caused by spurious solar responses as it is common for the LEMS30 detector, and it does not exist in the *Ulysses* LEMS120 measurement due to its orientation (e.g., Lanzerotti et al. 1992; Marhavilas et al. 2015). After February 22, the flow speed begins to decrease until $\sim$February 25, 00:00 UT, when there is a sudden jump in flow velocity, temperature, and IMF magnitude that indicates a forward wave (FW), since it was not identified as a shock in the IS database (http://ipshocks.fi/database). Around February 25–29, a forward wave–reverse wave (FW–RW) pair is observed, with an embedded MC that has been identified by several studies (e.g., Ebert et al. 2009; Du et al. 2010; Richardson 2014). The dominant MC signatures in this event are bidirectional electrons, abnormally low proton temperature T_p and beta β_p, enhanced magnetic field strength and total pressure, and smooth rotation in the polar angle (ϕ) of the magnetic field. The automatic GS reconstruction that we implement also successfully identifies this large-scale magnetic flux rope structure during the period of February 25, 22:25 UT–February 27, 09:19 UT, which is very similar to those discussed in previous reports (Ebert et al. 2009; Richardson 2014). We discuss the reconstructed cross-section map of this large-scale MC in detail in Section 5. A tangential discontinuity (not shown in Figure 1) is located at the edge of the MC, across which the total pressure is balanced. The FW–RW pair is excluded from the IS database, probably because the transition regions for both waves are broad, indicating that they may be mediated by energetic particles (e.g., Axford et al. 1982; Mostafavi et al. 2017). The enhancement of low-energy particles in this period is consistent with the predictions of DSA, since the particle flux exhibits an exponential decay upstream of the forward and reverse waves (e.g., Verkhoglyadova et al. 2015). The MC causes the falloff of particle flux, since the energetic particles produced at the shock/wave or the

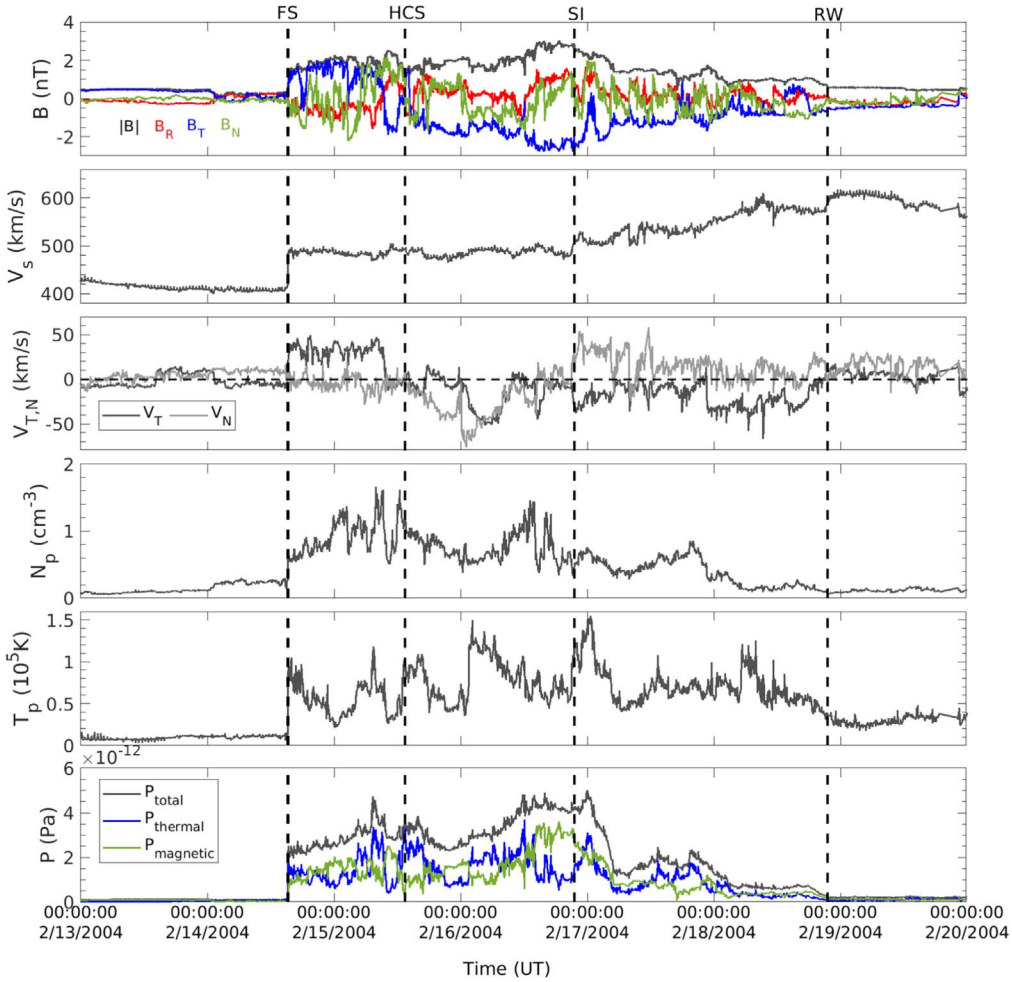

Figure 2. Parameters near the first SIR. The six panels show, from top to bottom, the magnetic field magnitude $|B|$ and the components B_R, B_T, and B_N; solar wind speed V_S; transverse solar wind velocity components V_T and V_N; proton number density N_p; proton temperature T_p; and thermal, magnetic, and total pressures. The location of the FS, HCS, SI, and RW is labeled by vertical dashed lines.

sheath region cannot easily penetrate the strong MC field (Cane & Lario 2006).

3. Evolution of the Energetic Particle Spectrum

The spectra of energetic particles provide us with important information about the acceleration processes. For example, the DSA mechanism predicts a PL spectrum for the velocity distribution function with an index $q = 3r/(r-1)$, where r is the shock compression ratio. The Zank et al. (2014) statistical transport theory for particles propagating in an environment comprising numerous magnetic islands predicts a PL-like spectrum downstream of the injection point in a certain energy range, and the spectral index is given by several parameters related to the turbulence and magnetic island properties, such as the particle diffusion coefficient κ, island contraction rate η_c, and strength of the reconnection electric field. The particle spectrum evolution behind the FS has been reported in Zhao et al. (2018b) and can be explained very well by a theoretical model that considers particle acceleration associated with numerous interacting magnetic islands. Zhao et al. (2018b) only showed the downstream spectra at eight specific times behind the shock. Here we present a more detailed analysis of the particle spectra over the whole period.

Figure 3 shows the energetic proton spectra measured by the *Ulysses* LEMS30 detector at 12 representative instances in panels (a)–(l), which are organized in chronological order. Here we use the 25 channel proton flux in the solar wind frame from the MFSA (M and F spectrum accumulator) analysis. The MFSA data have been background-corrected and converted to physical units (particle differential flux). They are available at 17 minute, 1 hr, and 1 day resolution through http://hiscale.ftecs.com/. We calculate 5 hr and 1 day averages using the 1 hr resolution data. For quiet-time spectra (panels (a) and (h)), we plot the 1 day averaged data. Otherwise, 5 hr averaged spectra are plotted to show more transient features. The energy range of the MFSA proton flux is 62.56–4428.47 keV. The energy band and average energy for each band can be found on the website and are not listed here. We plot the average energy for each channel as the representative energy, and each energy range is given by the corresponding error bar. Note that the flux data are not always available for all 25 channels. We simply skip the energy channel when no data are available for the channel during the period of averaging. To understand the spectral evolution, a linear fit is applied when a PL shape is exhibited in a certain energy range, and the corresponding PL index is obtained. Panel (a) shows an example of the quiet-time particle spectrum between February 13 and 14. The spectrum does

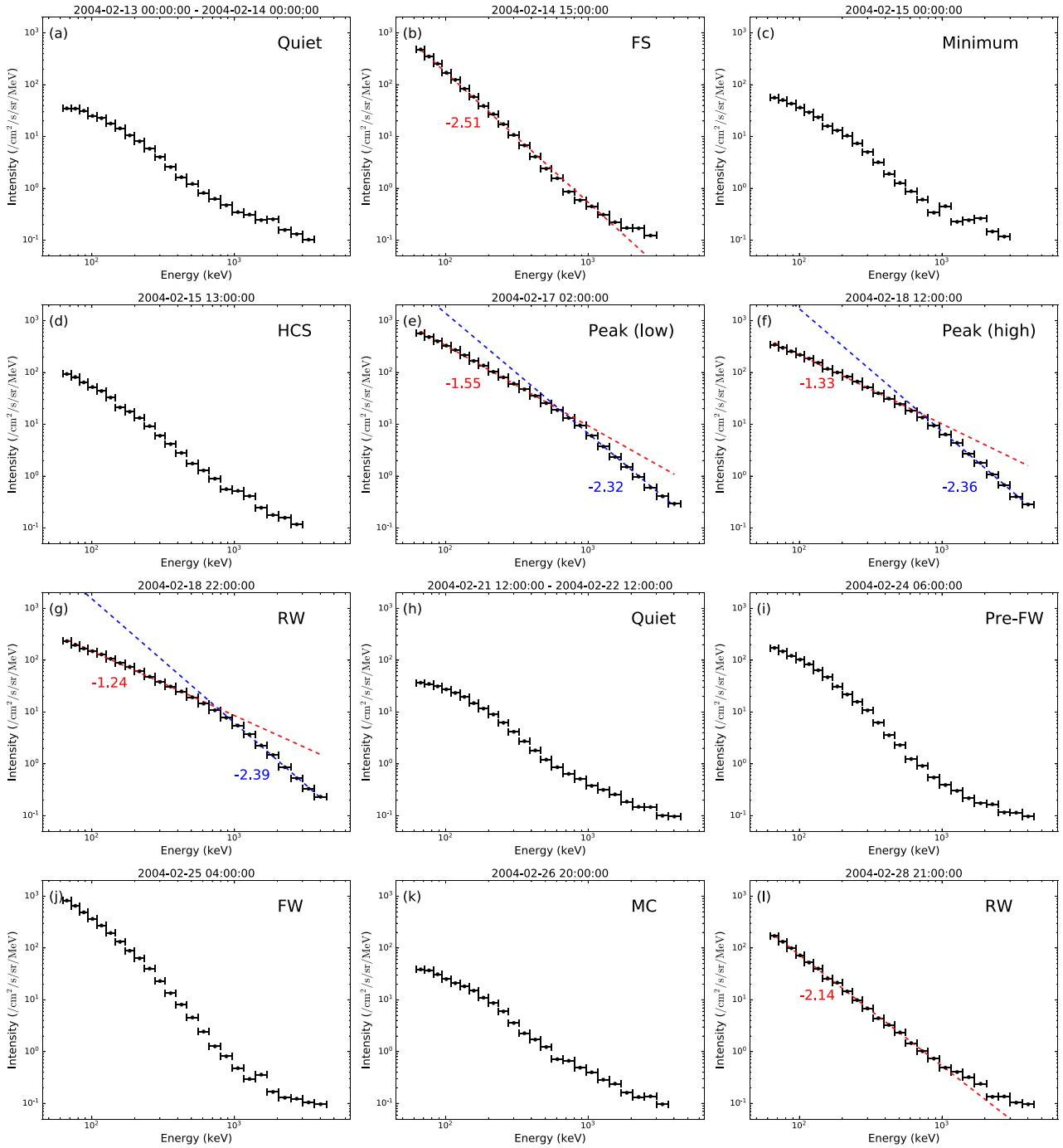

Figure 3. Energetic proton spectra at 12 instances over the energy range 62.56–4428.47 keV. Panels (a)–(l) show, in chronological order, the spectrum at (a) quiet time, (b) the forward shock (FS), (c) the local minimum behind the FS, (d) the heliospheric current sheet (HCS), (e) the intensity peak of low energies, (f) the intensity peak of high energies, (g) the reverse wave (RW), (h) quiet time, (i) ∼1 day ahead of the forward wave (FW), (j) the forward wave (FW), (k) the magnetic cloud (MC), and (l) the reverse wave (RW). A linear fit is applied when the spectrum exhibits a power-law shape, and the resulting spectral index is shown.

not exhibit a PL shape as there is a bump below ∼400 keV, which may indicate a rollover due to the effect of solar modulation (e.g., le Roux et al. 1999; Reames 2013). Panel (b) shows that at the FS arrival time, 15:00 UT, 2004 February 14, the lower end of the particle spectrum is enhanced dramatically and the spectrum looks like a PL except for the two highest energy channels. The best-fit PL index is calculated to be −2.51 using the lowest 21 channels (62.56–1694.76 keV). The number is quite far from the DSA prediction of −1.5, using the observed shock compression ratio $r = 2.5$. This suggests that DSA may not be fully applicable to explain the spectrum.

As discussed by Zhao et al. (2018b), the observed energetic particle intensities are further enhanced behind the shock. Here, we illustrate the evolution of the spectrum downstream of the FS in panels (c)–(g). Panel (c) shows the spectrum at 0:00, 2004 February 15, 9 hr after the FS passage when the low-energy particle flux decreased to a local minimum. The spectral shape is close to the quiet-time spectrum (panel (a)), with only a slight enhancement in a few channels. After this point,

particle fluxes increase in all energy channels. For example, panel (d) shows the spectrum near the HCS crossing at ~13:00, 2004 February 15, where there is a slight increase for all energies compared to panel (c). Another interesting phenomenon in this region is that medium- to high-energy particles are energized relative to the shock, while low-energy particle fluxes do not show much difference as shown in panels (e) and (f). The low-energy particle fluxes reach their maximum at ~2:00 UT on February 17 (panel (e)) and then start to decrease. However, the high-energy particle fluxes continue increasing until ~12:00 UT on February 18, when they reach peak intensities as shown in panel (f). The observed increase in distance between the particle intensity peak and the shock front with increasing energy is successfully predicted by the Zank et al. (2014) statistical transport theory for energetic particle interaction with numerous magnetic islands. The spectrum at the SIR reverse wave is plotted in panel (g). Although the particle intensities have dropped slightly from panel (f), the spectrum becomes a little harder as the low-energy particle fluxes decrease more rapidly. The spectra in panels (e)–(g) exhibit a double PL shape. Thus, we fit separately the lowest 15 channels (62.56–665.51 keV) and the highest 9 channels (799.67–4428.47 keV) with a PL. The PL indices for the low-energy part show a trend of hardening (changing from −1.55 to −1.24) during this period, while the high-energy part is slightly steepened (from −2.32 to −2.39). The strong enhancement of the particle flux and the hardening of the spectrum behind the shock suggest that flux rope compressional acceleration may be important. The acceleration seems to be more pronounced for particles with up to ~700 keV energy.

Panel (h) illustrates that the particle activity has returned to the quiet level at 12:00 UT, February 21–12:00 UT, February 22, with a spectrum resembling panel (a). The particle fluxes start increasing again around February 23 due to the acceleration by the FW. For example, in panel (i) at 06:00 UT on February 24, the low-energy particle fluxes have clearly increased. Panel (j) shows that at 05:00 UT on February 25, when the FW arrived, the low-energy particle fluxes are again strongly enhanced. However, we do not fit a PL spectrum as it is not as pronounced as at the FS in panel (b). After the passage of the FW, particle fluxes start to decrease as *Ulysses* approaches the MC structure. An example of the spectrum inside the observed MC is shown in panel (k), where the particle intensity drops to a background similar to the levels in panels (a) and (h). Finally, we show in panel (l) that the spectrum at 21:00 UT on February 28 near the second RW exhibits a PL shape excluding highest energies. The spectral index is calculated to be −2.14 using the lowest 18 energy channels (62.56–1161.50 keV), which indicates a spectrum that is harder than the spectrum at the FS (panel (b)).

To summarize, the particle spectrum analysis suggests that PL spectra are observed over the energy range ~60 keV–2.0 MeV near the arrival time of the shock and reverse compressional wave. However, the spectra near the shock or wave appear to be too soft to be explained by the DSA mechanism. The region of unusual particle flux enhancement behind the FS exhibits a double PL, and we show the hardening of the spectrum for energies below ~0.7 MeV, indicating additional acceleration mechanisms besides DSA. We show in Sections 4 and 5 that the enhanced generation of magnetic islands, which are believed to be coherent quasi-2D structures of evolving (dynamical) solar wind turbulence, may be responsible for the additional particle acceleration.

4. PSD Analysis

Diffusion plays an important role in the energization of particles, for both classical DSA and stochastic acceleration by magnetic reconnection or islands (e.g., Zank et al. 2014). The DSA mechanism requires that particles scatter and propagate diffusively across the shock multiple times. Small-scale magnetic islands may act like scattering centers, causing the diffusion and acceleration of particles. In the supersonic solar wind, particle diffusion is typically associated with magnetic turbulence that is convected with solar wind flow (e.g., Zhao et al. 2017). Early test-particle simulations suggested that turbulence produces magnetic "bubbles," which can trap particles in the strong reconnection electric field for a sufficiently long time, and thus produce significant particle acceleration (Matthaeus et al. 1984; Goldstein et al. 1986; Ambrosiano et al. 1988). It is therefore very useful to analyze the properties of magnetic turbulence during the period of interest. We carry out a PSD analysis of the magnetic field fluctuations (e.g., Leamon et al. 1998; Hu et al. 2013) using 1 s resolution *Ulysses* magnetic field components (RTN) and magnitude data for the FS–RW and FW–RW pairs. We select a time interval from 1.5 days before to 5 days after the FS (around February 14, 15:15 UT) and plot the evolution of the magnetic field power spectrum in panel (a). The analysis is based on the Fourier-transformed autocorrelation tensor of the three magnetic field components, from which the PSD is taken as its trace (Leamon et al. 1998):

$$\mathrm{PSD} = \mathcal{F}\{b_R b_R' + b_T b_T' + b_N b_N'\},$$

where $\mathcal{F}$ denotes the Fourier transformation and $b_R b_R'$, $b_T b_T'$, and $b_N b_N'$ are the autocorrelation functions of the fluctuations in the three magnetic field components, respectively. The dashed and solid lines are examples of the power spectra upstream and downstream of the shock, respectively, and they are color-coded by the normalized distance to the shock front (0 represents the shock front and 1 represent the points farthest away from the shock, either upstream or downstream). Each power spectrum is calculated in a 3 hr sliding window with possible overlapping between adjacent intervals up to 75%. Assuming the turbulence convected with the solar wind flow, we use the Taylor hypothesis to convert the frequency ν to wavenumber k: $k = 2\pi\nu/|v_{\mathrm{sw}}|$. The magnitude of the solar wind speed $|v_{\mathrm{sw}}|$ is calculated by averaging over each 3 hr window. Proton gyrofrequencies are calculated using the mean magnetic field (1 day averaged) both upstream and downstream of the shock. The corresponding wavenumbers from the 1 day averaged upstream and downstream velocities are identified by the vertical dashed line (upstream) and solid line (downstream), respectively. A Kolmogorov $k^{-5/3}$ spectrum is displayed for reference. Similarly, we select a time interval from 1.5 days before to 5 days after the identified FW front (around February 25, 04:00 UT), and the results are plotted in panel (b). Both intervals include the corresponding RW fronts.

From Figure 4(a), we find that both upstream and downstream spectra exhibit a near Kolmogorov-like shape over the considered wavenumber range. The upstream spectra show some flattening at large wavenumbers (~10^{-3} km^{-1}), which

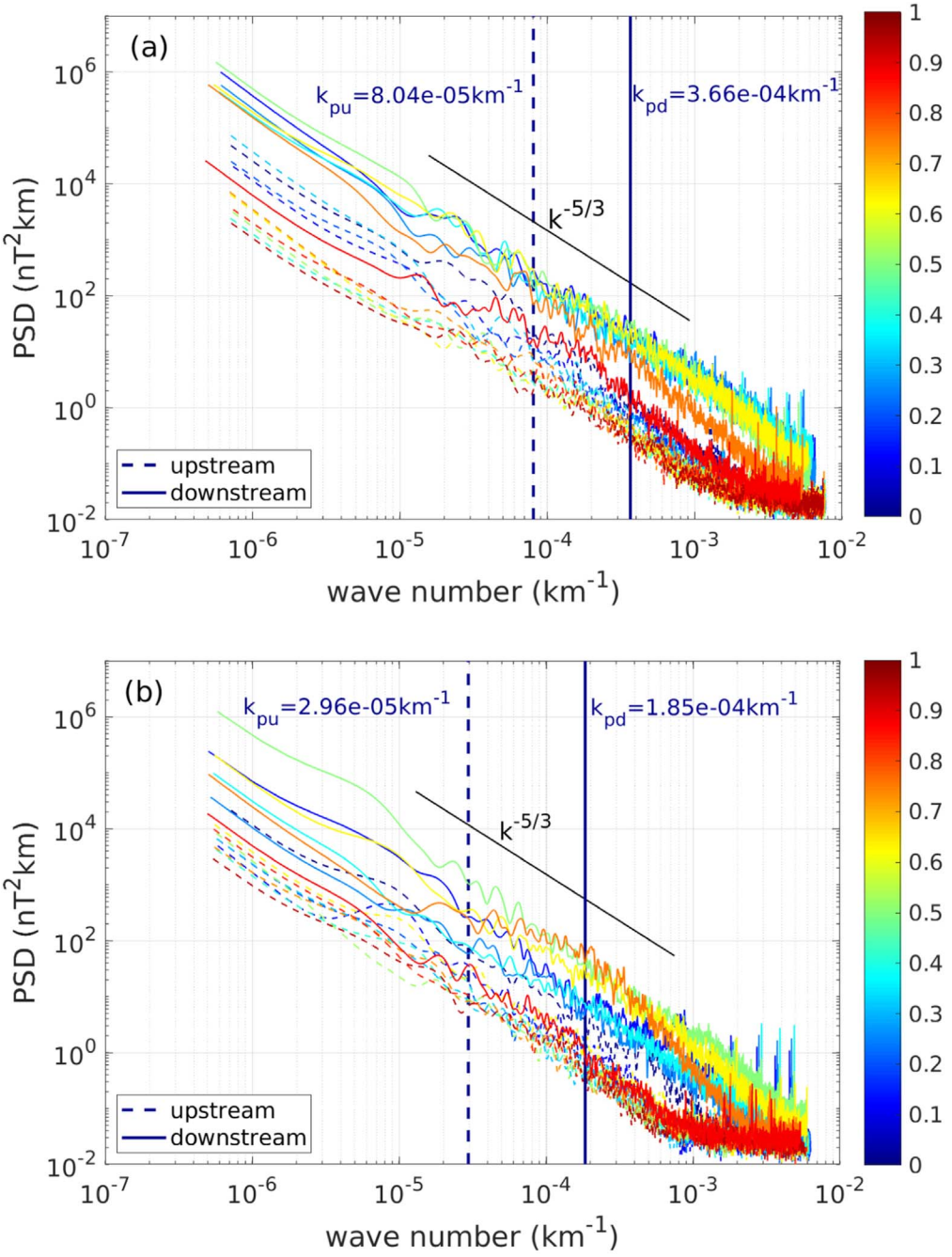

Figure 4. A typical sliding-window PSD analysis of the magnetic field fluctuations for the two FS/FW–RW pairs. The two panels plot the time between 1.5 days before and 5 days after the FS (panel (a)) and the FW (panel (b)) crossing. The dashed lines represent the upstream spectra and the solid lines the downstream spectra. The vertical lines identify the wavenumbers corresponding to the proton gyrofrequencies upstream (dashed line) and downstream (solid line). A Kolmogorov-like $k^{-5/3}$ spectrum is displayed for reference.

may be attributed to instrumental noise (Chen 2016). The power is clearly larger downstream of the FS and returns to lower levels after passing the reverse wave, which is what one would expect since the shock amplifies the turbulence level (Lu et al. 2009; Adhikari et al. 2016). We also find that the magnetic field power increases when it gets closer to the shock from upstream. Observations of upstream wave activity have been reported by Bamert et al. (2004), who suggested that the waves can scatter particles back to the shock. The shock we observed is quasi-perpendicular with a shock normal angle of ∼50°. Although quasi-perpendicular shocks typically suppress the excitation of upstream waves, the observed shock is quite oblique and thus cannot completely quench the upstream turbulence (e.g., Zank et al. 2006). As shown in Figure 4(b), although there is no shock identified for the later FW–RW pair (around February 25, 00:00 UT–February 29, 00:00 UT), we find a trend similar to the magnetic power increases within the FW–RW pair. An interesting feature is that the power spectrum just upstream of the RW has a bump near the proton gyrofrequency (see the orange solid line in panel (b)), which indicates some wave activity. This is consistent with the observation of enhanced wave power immediately upstream of a shock (Bamert et al. 2004) and may be important for the scattering of accelerated particles. The increasing wave activity

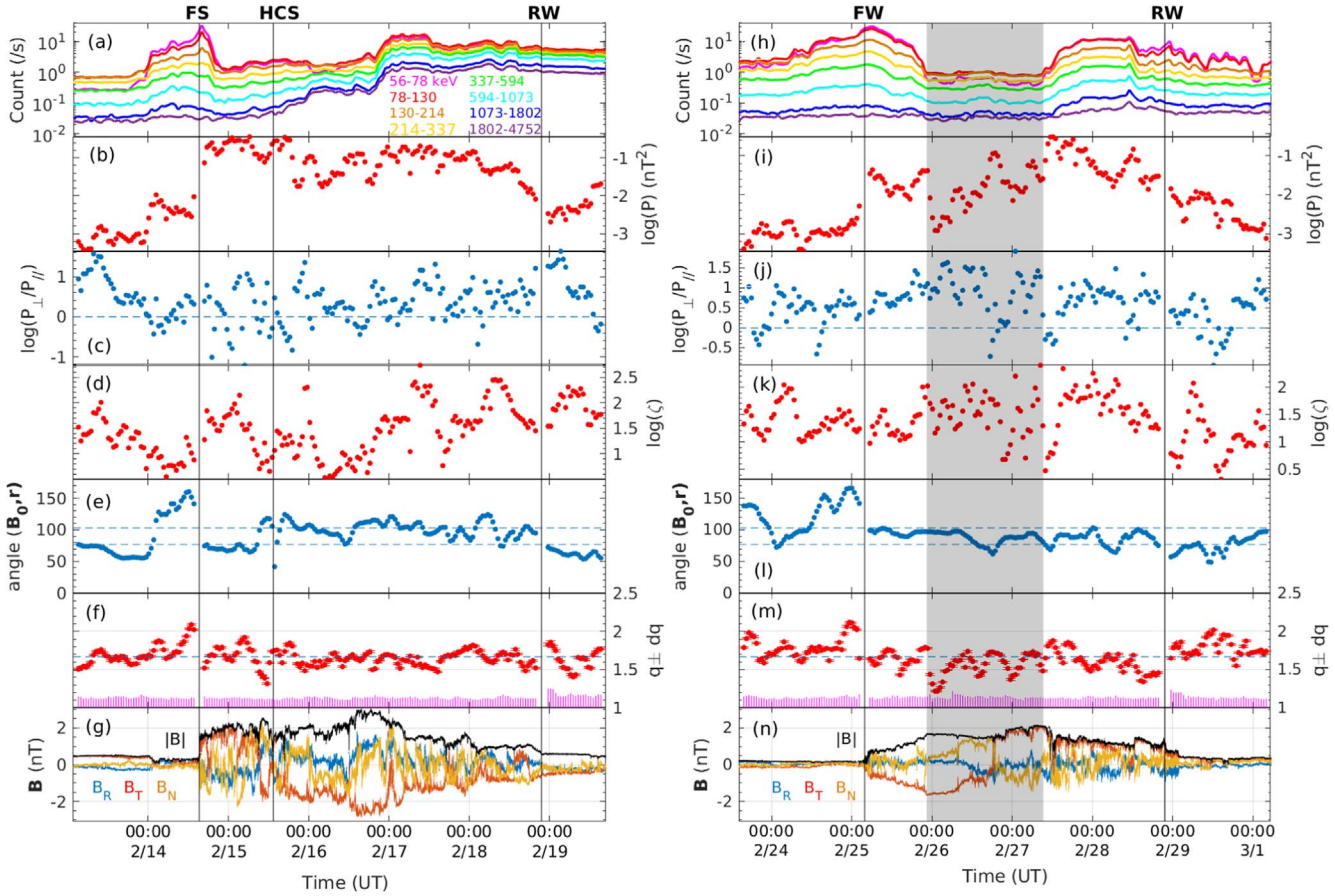

Figure 5. PSD analysis of the selected intervals. Panels (a)–(g) show the results for the first FS–RW interval and panels (h)–(n) for the second FW–RW interval. The vertical lines represent the crossing time of the FS, HCS, the first RW, FW and the second RW. The magnetic cloud in the second interval is denoted by the shaded area. From top to bottom, the seven panels show the ion count rates, the total power in the magnetic field fluctuation, the ratio between the power in perpendicular and parallel fluctuations, the ζ parameter defined by the ratio between the trace of the Fourier-transformed autocorrelation tensor over the fluctuation power in the magnetic field magnitude, the angle between the background magnetic field and the radial direction, power-law indices and χ^2-estimated uncertainties, and the components and magnitude of the magnetic field. Note that panels (b)–(d) and (h)–(j) are plotted as logarithms (base 10) of the corresponding quantities.

is also consistent with the interpretation of the FW and RW as energetic particle mediated shocks (e.g., Mostafavi et al. 2017).

Figure 5 shows a detailed analysis of the PSD in the two selected intervals corresponding to Figure 4. Panels (a)–(g) show the results for the first FS–RW pair and panels (h)–(n) for the second FW–RW pair. The vertical lines indicate the location of the FS, HCS, the first RW, FW, and the second RW structures as discussed in Section 2. Panels (b)–(d) and (i)–(k) are plotted as logarithms (base 10). Panels (a) and (h) are the LEMS30 ion count rates corresponding to those shown in Figure 1. Panels (b) and (i) show the total power in magnetic field fluctuations corresponding to the first FS–RW interval and the second FW–RW interval, respectively. The total power is calculated by integrating the PSD over the considered frequency range:

$$P_{\rm total} = \int d\nu {\rm PSD}(\nu).$$

It indicates that the magnetic field fluctuation power increases by ~2 orders of magnitude after the FS or FW crossing and decreases across both RWs. This further confirms our finding from Figure 4. Panels (c) and (j) show that the ratio between the perpendicular and parallel power $P_\perp/P_\parallel$ is larger than 1 (the horizontal dashed line; note the logarithm in the vertical axis) most of the time, suggesting that most of the power resides in the transverse fluctuations. This is consistent with nearly incompressible MHD turbulence models (e.g., Zank & Matthaeus 1992, 1993; Hunana & Zank 2010; Zank et al. 2017), which suggest that the solar wind turbulence is composed of a majority of 2D fluctuations and a minority of slab fluctuations, both of which are transverse to the background magnetic field. The decomposition of the parallel and perpendicular power is based on the background magnetic field direction determined by a minimum variance analysis (MVA) technique (Sonnerup & Scheible 1998; Zhao et al. 2018a) for each 3 hr window. The ratio $P_\perp/P_\parallel$ decreases slightly behind the FS, suggesting that the shock generates preferentially parallel fluctuations. The $P_\perp/P_\parallel$ ratio is typically used as a proxy for the magnetic compressibility (e.g., Alexandrova et al. 2008; Gary & Smith 2009; Salem et al. 2012; Burlaga et al. 2018): a smaller ratio suggests stronger compression, which may support the flux rope related compressive acceleration of energetic particles (Zhao et al. 2018b). The trend is reversed for the second interval as the ratio increases slightly within the second FW–RW pair. We also find that the $P_\perp/P_\parallel$ value is somewhat larger during this interval. The reason may be related to the properties of the shock/wave, or the presence of the HCS versus MC. Panels (d) and (k) plot the

parameter ζ, which is defined as the ratio between the total power in the magnetic field fluctuations $P_{\rm total}$ and the power in the fluctuations of the magnetic field magnitude $P_{\rm mag}$ (e.g., Horbury & Schmidt 1999):

$$\zeta = \frac{P_{\rm total}}{P_{\rm mag}} = \frac{\int d\nu \mathcal{F}\{b_R b_R' + b_T b_T' + b_N b_N'\}}{\int d\nu \mathcal{F}\{|b||b|'\}}.$$

Here, $|b||b|'$ is the autocorrelation function of the magnitude of the magnetic field. It shows a similar trend to the $P_\perp/P_\parallel$ ratio. However, we caution the reader that the PSD analysis is based on the assumption of magnetostatic turbulence, so both the $P_\perp/P_\parallel$ ratio and the ζ parameter are not directly related to the dynamics of flux ropes. Panels (e) and (l) show the angle between the background magnetic field direction (decided by MVA) and the radial direction. For the first FS–RW interval, the background magnetic field is mostly along the normal Parker field directions, which are illustrated by the horizontal dashed lines in panel (e). We notice that the field direction deviates from the Parker field direction ~1 day before the shock arrival, which coincides with a CS crossing as we have discussed in Section 2. After the shock crossing, the background field direction returns to the direction far upstream, and then reverses again near February 15, 12:00 UT—this field reversal corresponds to the HCS crossing. For the second FW–RW interval, the background field direction is not well aligned with the Parker field upstream of the FW, but they are well aligned downstream. As we have already shown in Figure 4, the magnetic field power spectra follows approximately a $k^{-5/3}$ PL. Here in panels (f) and (m), we show the PL indices obtained by fitting the spectra with χ^2-estimated uncertainties. The frequency range we choose is 0.001–0.06 Hz, which lies in the middle of the spectra and is illustrated by the line-of-reference Kolmogorov spectrum shown in Figure 4. The values of $1 + \chi_r^2$ are plotted as vertical magenta lines at the bottom of panels (f) and (m), where $\chi_r^2 = \chi^2/N_f$ is the reduced χ^2 with N_f the degree of freedom. A small χ_r^2 (close to zero) means a small fitting residue. Our result shows that the actual χ_r^2 is close to zero for each window, meaning the data are consistent with the PL model. For both intervals, we find that the absolute value of the PL index q gradually increases and becomes larger ($q \sim -2$) a few hours before the FS and FW. This corresponds to the enhanced turbulence with a possible departure from a Kolmogorov-like power spectrum immediately upstream of the FS and FW. This behavior is consistent with the excitation of upstream waves by the streaming instability invoked for quasiparallel shocks and DSA (e.g., Gordon et al. 1999; Rice et al. 2003). Finally, as a reference, panels (g) and (n) show the RTN components and magnitude of the magnetic field.

It should be pointed out that in a two-component MHD turbulence model, the wave vector $\boldsymbol{k}$ for the slab component is parallel to the background magnetic field $\boldsymbol{B}_0$ and is perpendicular to $\boldsymbol{B}_0$ for the 2D component (Zank & Matthaeus 1992, 1993; Bieber et al. 1996; Zank et al. 2017). Typically at ~5 au, the solar wind velocity is almost perpendicular to the spiral IMF, as is also indicated by our Figures 5(e) and (l) since the solar wind velocity is mostly radial. Therefore, the spacecraft measures mostly 2D rather than slab fluctuations. Since flux ropes are considered to be quasi-2D structures, the increasing power in magnetic field fluctuations within the SIR is consistent with the generation of magnetic flux ropes. We caution that the PSD analysis assumes explicitly that the turbulence is convected with the solar wind flow, which is an obvious caveat of the method. Nevertheless, it is very informative especially in the absence of multispacecraft measurements.

5. Reconstruction of Magnetic Flux Ropes

The PSD analysis presented in Section 4 suggests that the enhanced turbulence level within the SIR may be an indication of the presence of small-scale magnetic flux ropes. More direct evidence for the presence of flux ropes can be provided by reconstructing their magnetic field structures. Here, we use an automated detection technique based on the GS reconstruction method (Hau & Sonnerup 1999; Hu et al. 2004; Zheng & Hu 2018) to detect these structures from in situ *Ulysses* data. Following Zheng & Hu (2018), the automated detection algorithm for small-scale flux ropes is based on the GS equation given by

$$\frac{\partial^2 A}{\partial x^2} + \frac{\partial^2 A}{\partial y^2} = -\mu_0 \frac{dP_t(A)}{dA} = -\mu_0 j_z(A). \quad (1)$$

Here, P_t is the total transverse pressure defined by $P_t = p + B_z^2/2\mu_0$, the sum of the plasma pressure and axial magnetic pressure, $A(x, y)$ is the magnetic flux function, and j_z is the axial current density. We require that P_t be a single-valued function of A, and the solution of A can be obtained over the cross-section plane (x, y) by solving Equation (1) once the function $P_t(A)$ is known. Since each field line or flux surface of a flux rope corresponds to a distinct A value during the specific time period, the determination of a flux rope configuration can be simplified to a series of calculations of P_t versus A. During this process, all data from the *Ulysses* measurements are transformed to a quasistationary frame, i.e., usually the de Hoffmann–Teller frame, which is essential for using the GS equation since the assumption of quasi-2D MHD equilibrium has to be approximately satisfied.

The main criterion of our detection algorithm is to verify the double-folding and single-valued behavior of the P_t versus A curve. When a spacecraft goes through a flux rope, it will pass the same set of magnetic field lines along one-half of the path from one edge of the flux rope to the center as it will along the other half of the path from the center to the other edge but in reverse order. We therefore split the spacecraft path into two branches (halves), and then calculate the P_t versus A values and check to see if the double-folding pattern exists and how well $P_t(A)$ being single-valued is satisfied. The center of the path is defined as the turning point of the $P_t(A)$ curve, where the transverse field component in the flux rope frame changes the sign. Detailed descriptions of the search procedures for small-scale flux ropes with a wide range of duration are documented in Hu et al. (2018). Below we provide a brief description of the search results of flux ropes with a wide duration range as applied to the *Ulysses* data for the time period 2004 February 13–March 3 near the ecliptic plane.

It is worth mentioning that the standard GS equation assumes a quasistatic equilibrium. In addition to the appropriate frame of reference, an extra threshold condition is necessary, which is the Walén slope, the ratio of the remaining flow

Table 1
List of Small-scale Flux Ropes from 2004 February 13 to March 3

No.	Time Range	Duration (minutes)	$\langle B \rangle$ (nT)	$V_{\rm SW}$ (km s^{-1})	$\langle \beta \rangle$	Scale Size (au)	Orientation (°)
1	2004 Feb 13 21:18–2004 Feb 14 05:30	493	0.3361	408.7881	1.2164	0.0715	$\theta = 110$, $\phi = 60$
2	2004 Feb 14 08:50–2004 Feb 14 10:58	129	0.2546	407.0208	1.4896	0.0209	$\theta = 140$, $\phi = 100$
3	2004 Feb 14 13:14–2004 Feb 14 14:58	105	0.2905	413.3684	1.0554	0.0162	$\theta = 130$, $\phi = 60$
4	2004 Feb 14 18:06–2004 Feb 14 19:21	76	1.6439	487.5580	0.5660	0.0140	$\theta = 130$, $\phi = 120$
5	2004 Feb 14 22:50–2004 Feb 14 23:35	46	2.0594	488.7090	0.2375	0.0088	$\theta = 120$, $\phi = 80$
6	2004 Feb 15 00:42–2004 Feb 15 01:56	75	2.0346	483.9880	0.3420	0.0141	$\theta = 100$, $\phi = 80$
7	2004 Feb 15 02:24–2004 Feb 15 05:44	201	1.9216	480.9900	0.5968	0.0276	$\theta = 120$, $\phi = 40$
8	2004 Feb 15 08:14–2004 Feb 15 12:26	253	2.0614	487.8778	0.5444	0.0475	$\theta = 30$, $\phi = 240$
9	2004 Feb 16 02:20–2004 Feb 16 03:11	52	1.6775	488.1244	0.8135	0.0048	$\theta = 100$, $\phi = 200$
10	2004 Feb 16 04:40–2004 Feb 16 20:28	949	2.2927	488.5959	0.5216	0.1864	$\theta = 100$, $\phi = 260$
11	2004 Feb 16 22:20–2004 Feb 17 00:45	146	2.2906	513.5441	0.5683	0.0292	$\theta = 70$, $\phi = 280$
12	2004 Feb 17 00:56–2004 Feb 17 06:03	308	1.9344	510.2289	0.3647	0.0616	$\theta = 80$, $\phi = 280$
13	2004 Feb 17 06:11–2004 Feb 17 07:07	57	1.4261	532.7164	0.2923	0.0120	$\theta = 100$, $\phi = 280$
14	2004 Feb 17 07:52–2004 Feb 17 10:06	135	1.4915	515.8932	0.3084	0.0244	$\theta = 70$, $\phi = 300$
15	2004 Feb 17 10:26–2004 Feb 17 11:15	50	1.4220	535.0386	0.4686	0.0093	$\theta = 100$, $\phi = 300$
16	2004 Feb 17 12:31–2004 Feb 17 13:18	48	1.4338	529.2614	0.6167	0.0100	$\theta = 70$, $\phi = 280$
17	2004 Feb 17 18:05–2004 Feb 17 21:01	177	1.1349	534.0142	1.3097	0.0341	$\theta = 120$, $\phi = 240$
18	2004 Feb 17 22:28–2004 Feb 17 23:14	47	1.6113	545.2787	0.3032	0.0100	$\theta = 110$, $\phi = 280$
19	2004 Feb 18 03:40–2004 Feb 18 04:31	52	0.8748	566.5741	0.6265	0.0097	$\theta = 50$, $\phi = 220$
20	2004 Feb 18 04:45–2004 Feb 18 08:14	210	0.9357	575.0715	0.5014	0.0406	$\theta = 80$, $\phi = 300$
21	2004 Feb 18 13:25–2004 Feb 18 18:23	299	1.0009	576.3612	0.3761	0.0557	$\theta = 140$, $\phi = 20$
22	2004 Feb 19 04:38–2004 Feb 19 06:38	121	0.5818	607.4526	0.2980	0.0290	$\theta = 120$, $\phi = 260$
23	2004 Feb 19 11:49–2004 Feb 19 15:13	205	0.4541	582.5760	0.9149	0.0473	$\theta = 110$, $\phi = 280$
24	2004 Feb 19 17:44–2004 Feb 19 18:51	68	0.4782	579.0347	0.5335	0.0137	$\theta = 80$, $\phi = 240$
25	2004 Feb 19 22:51–2004 Feb 20 08:45	595	0.4838	556.2728	0.5276	0.1321	$\theta = 50$, $\phi = 260$
26	2004 Feb 20 09:00–2004 Feb 20 09:46	47	0.3656	560.7113	0.9349	0.0105	$\theta = 40$, $\phi = 280$
27	2004 Feb 20 11:19–2004 Feb 20 13:36	138	0.3424	551.4694	1.0022	0.0301	$\theta = 50$, $\phi = 280$
28	2004 Feb 20 17:37–2004 Feb 21 00:11	395	0.5423	592.7347	1.0389	0.0726	$\theta = 60$, $\phi = 320$
29	2004 Feb 21 00:20–2004 Feb 21 01:07	48	0.4762	593.9766	0.6582	0.0113	$\theta = 50$, $\phi = 260$
30	2004 Feb 21 03:59–2004 Feb 21 05:08	70	0.5185	601.3837	0.2248	0.0155	$\theta = 60$, $\phi = 300$
31	2004 Feb 21 06:31–2004 Feb 21 07:48	78	0.5298	592.5363	0.2659	0.0184	$\theta = 80$, $\phi = 280$
32	2004 Feb 21 10:48–2004 Feb 21 12:50	123	0.4910	592.3417	0.2373	0.0288	$\theta = 120$, $\phi = 260$
33	2004 Feb 21 13:42–2004 Feb 22 00:09	628	0.4170	590.2301	0.9897	0.1309	$\theta = 80$, $\phi = 240$
34	2004 Feb 22 09:47–2004 Feb 22 13:54	248	0.3386	590.9667	0.8512	0.0530	$\theta = 110$, $\phi = 240$
35	2004 Feb 22 20:06–2004 Feb 22 20:56	51	0.2453	567.7555	2.2971	0.0115	$\theta = 170$, $\phi = 40$
36	2004 Feb 22 21:14–2004 Feb 22 22:51	98	0.2923	565.2687	1.4281	0.0218	$\theta = 60$, $\phi = 280$
37	2004 Feb 22 23:47–2004 Feb 23 00:46	60	0.2567	565.2222	1.3173	0.0121	$\theta = 80$, $\phi = 240$
38	2004 Feb 23 02:07–2004 Feb 23 05:54	228	0.2288	558.0575	0.8635	0.0480	$\theta = 40$, $\phi = 300$
39	2004 Feb 23 07:46–2004 Feb 23 10:11	146	0.2132	547.2537	0.5433	0.0317	$\theta = 70$, $\phi = 260$
40	2004 Feb 23 10:25–2004 Feb 23 11:26	62	0.2144	544.0406	0.4979	0.0134	$\theta = 70$, $\phi = 260$
41	2004 Feb 23 14:03–2004 Feb 23 16:36	154	0.2039	537.5287	0.5346	0.0208	$\theta = 100$, $\phi = 320$
42	2004 Feb 25 16:25–2004 Feb 25 19:51	207	1.1995	576.6879	0.4221	0.0476	$\theta = 80$, $\phi = 280$
43	2004 Feb 25 20:07–2004 Feb 25 21:46	100	1.4322	575.453	0.1625	0.0230	$\theta = 70$, $\phi = 280$
44	2004 Feb 25 22:25–2004 Feb 27 09:19	2095	1.6895	548.6536	0.1415	0.3690	$\theta = 40$, $\phi = 160$
45	2004 Feb 27 11:55–2004 Feb 27 13:04	70	1.0032	529.3672	2.3685	0.0092	$\theta = 120$, $\phi = 20$
46	2004 Feb 27 23:28–2004 Feb 28 06:38	431	1.2188	526.3701	0.6774	0.0894	$\theta = 80$, $\phi = 100$
47	2004 Feb 28 10:54–2004 Feb 28 12:32	99	0.9888	525.2929	1.1800	0.0165	$\theta = 40$, $\phi = 20$
48	2004 Feb 29 09:47–2004 Feb 29 17:34	468	0.2794	588.2252	1.6508	0.0980	$\theta = 60$, $\phi = 120$
49	2004 Mar 1 06:54–2004 Mar 1 10:35	222	0.3537	579.0119	0.2753	0.0481	$\theta = 50$, $\phi = 60$
50	2004 Mar 1 12:45–2004 Mar 1 14:27	103	0.3524	568.6931	0.2952	0.0233	$\theta = 70$, $\phi = 80$
51	2004 Mar 1 19:03–2004 Mar 1 19:54	52	0.3497	566.7363	0.2253	0.0117	$\theta = 100$, $\phi = 100$
52	2004 Mar 2 11:13–2004 Mar 2 13:11	119	0.3547	561.3957	0.1782	0.0265	$\theta = 100$, $\phi = 100$

velocity to the local Alfvén velocity. We apply a small Walén slope threshold condition to exclude Alfvénic structures and waves and ensure that the quasistatic condition is satisfied.

After completing the searching for the whole year of 2004, we found a total of 52 small-scale flux ropes for this time period with their intervals marked as gray shadows in Figure 1. The parameters of these small-scale flux ropes are presented in Table 1, which can be summarized as follows. (1) The time range marks the starting and ending times of each flux rope interval. (2) The duration is the total time it takes for the *Ulysses* spacecraft to pass through a flux rope. The shortest one in this time period is 46 minutes while the longest one is 2095 minutes corresponding to the MC event. (3) The average magnetic field magnitude and solar wind speed are calculated in each flux rope interval with the smallest magnitude and speed being $\sim$0.2 nT and $\sim$400 km s^{-1}, respectively. The largest ones are $\sim$2.3 nT and $\sim$600 km s^{-1}, respectively. (4) The average plasma proton beta varies from $\sim$0.14 to $\sim$2.37.

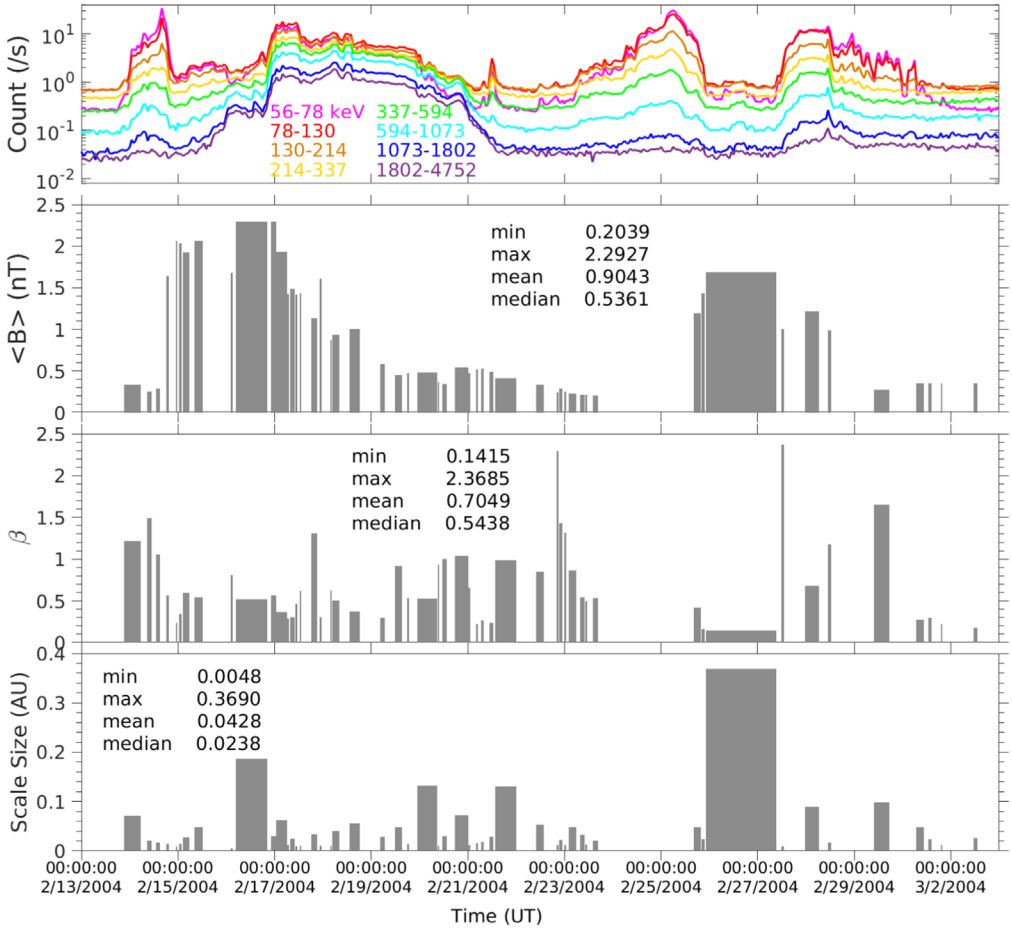

Figure 6. Distributions and statistics of reconstructed flux rope parameters are shown in the bottom three panels. The width of each column represents the duration of each flux rope, and the vertical axes show, from top to bottom, the mean magnetic field $\langle B \rangle$, mean plasma beta β, and scale size. The minimum, maximum, mean, and median values of each parameter are shown in the figure. The ion count rate data is plotted in the top panel.

(5) Scale size is obtained in the flux rope frame, which indicates the spatial extent of the flux rope cross-section along the spacecraft path. It varies from ∼0.005 to ∼0.37 au and covers a wide range. Notice that flux rope #9 in Table 1 with the smallest scale size also has a relatively shorter duration while the largest flux rope #44 has the longest duration although the relation between duration and scale size is not linear. (6) The axis orientation is given by two angles: the polar angle θ, which is the angle between the z-axis (given in the RTN coordinate system) and the N direction, and the azimuthal angle ϕ, which is measured from the positive R direction toward the projection of the z-axis onto the RT plane. Figure 6 illustrates the variation of selected parameters for all flux ropes during the period of interest including the mean magnetic field $\langle B \rangle$, proton beta β, and scale size for each identified flux rope interval. Each gray column in the figure represents the corresponding parameter value for the reconstructed flux rope with its duration represented by the width. The minimum, maximum, mean, and median values of each parameter are also given in each panel. As a reference, we include again the ion count rate data in the top panel. Figure 6 shows that numerous small-scale flux ropes appear to coincide with strong particle acceleration during the HCS/SIR period and the large-scale MC suppresses the energetic particle flux. The second-largest flux rope on February 16 may also suppress the acceleration processes, which corresponds to an increase in particle intensity (or decrease away from the acceleration region) at its right boundary. Unlike the well-defined MCs (i.e., large-scale flux ropes), which possess the property of ultra-low plasma β, as exemplified by flux rope #44 in Table 1, the plasma β for small-scale flux ropes is more significant in magnitude and exhibits no general trend (Hu et al. 2018). Small-scale flux ropes are typically characterized by an elevated magnetic field magnitude in their core regions, i.e., local broadly defined maxima in time-series measurements. They are believed to be bounded by discontinuities or CSs (e.g., Zheng & Hu 2018). Such boundaries are clearly visible as delineated in Figures 1 and 6. Several boundaries coincide well with abrupt and significant changes in particle flux as demonstrated in the top panel of Figure 1, which is consistent with previous findings (e.g., Tessein et al. 2016; Greco et al. 2018). These studies reported the coincidence in the occurrence of discontinuities and particle flux changes, and implied particle trapping and energization by coherent structures. We provide a more detailed analysis of such a scenario. Given the limitation of the single-point or single-line measurements across a "sea" of flux ropes separated by CSs, it is difficult to directly correlate the signatures between energetic particle flux and flux rope properties. However, it is worthwhile to pursue such a study via a statistical approach by examining a large number of events with relevant observations.

Since our searching window has been extended to 42 hr compared to previous studies (Hu et al. 2018; Zheng & Hu 2018), large-scale flux ropes are included in our event list as

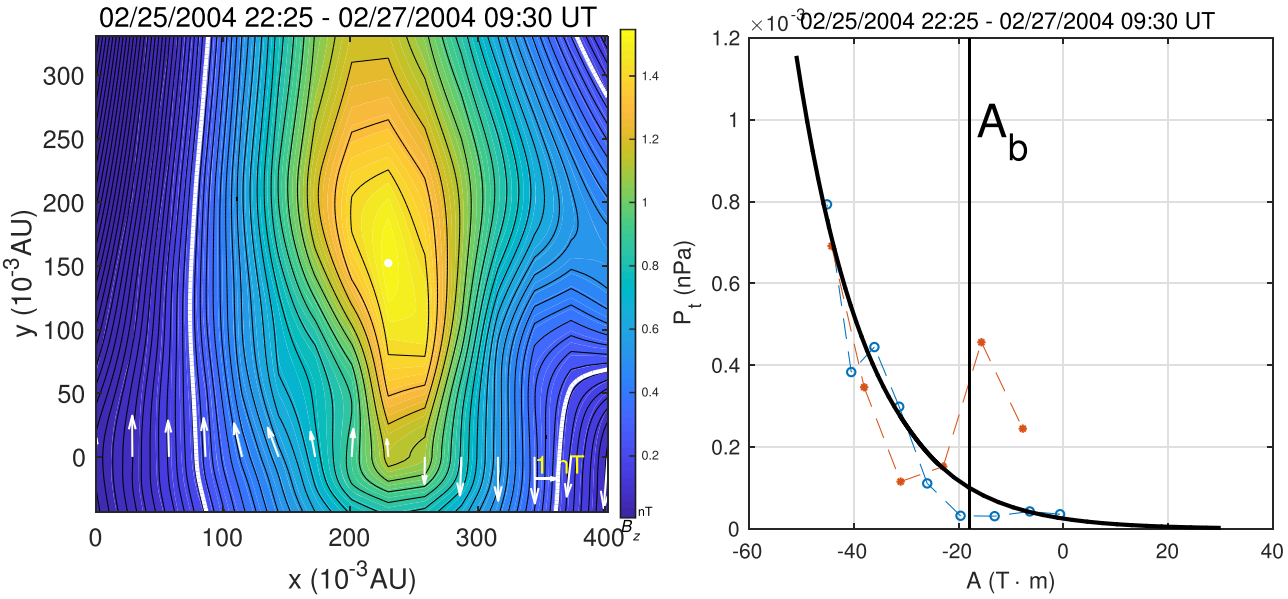

Figure 7. The reconstruction map and P_t vs. A curve of flux rope #44 (2004 February 25, 22:25 UT–2004 February 27, 9:19 UT) in Table 1. In the left panel, the cross-section is plotted with the transverse magnetic field (marked as black contour lines) and the axial magnetic field B_z (shaded color). The flux rope center corresponding to the maximum of B_z is denoted by the white dot, and the projected field vectors along the spacecraft path at $y = 0$ are shown by white arrows. In the right panel, the P_t vs. A fitting curve is shown by the black solid line, and the two aforementioned branches are plotted as blue circles and orange dots. The vertical line denoted by A_b indicates the boundary of the flux rope, which corresponds to the white solid contour in the left panel.

well. For example, the event starting from 2004 February 25, 22:25 UT, to 2004 February 27, 09:19 UT (#44 in Table 1), matches one MC interval identified by Ebert et al. (2009; 2004 February 25, 22:00 UT–2004 February 27, 10:00 UT) and Richardson (2014; 2004 February 25, 19:00 UT–2004 February 27, 11:00 UT). Figure 7 shows the cross-section map (left panel) and P_t versus A curve for this large-scale flux rope based on the GS reconstruction. In the left panel, we plot the in-plane magnetic field lines (black solid lines) of the reconstructed flux rope cross-section and the axial magnetic field B_z in color with scales given by the color bar. The white dot is the center of the flux rope, and the white arrows represent the transverse magnetic field vectors along the *Ulysses* path ($y = 0$). The right panel shows the calculated P_t versus A as blue circles and orange dots for the two branches (coming into and out of the flux rope, respectively). The vertical line A_b is the boundary within which the measured P_t versus A shows a clear double-folded pattern, and it corresponds to the thick white contour in the left panel. We use a polynomial function to fit the P_t versus A curve in the double-folded region and extrapolate it for the range outside of the spacecraft data, as shown by the black solid line. The fitted and extrapolated curve is then used for computing the reconstructed cross-section map in the left panel. In the case of the MC, we find that its scale size is 0.369 au and the duration is 2095 minutes. We note that there are still discrepancies in event intervals from the two lists cited above due to the different selection criteria for flux ropes as applied to searching. However, it is remarkable that the result of our automatic detection is within 2 hr from the manually selected *Ulysses* ICME event, and both the average field magnitude and solar wind speed agree well.

To further illustrate the existence and variabilities in the small-scale flux rope configuration based on the GS reconstruction results, the cross-section maps of 12 selected flux ropes are presented in Figure 8 in the same format as the left panel of Figure 7. A wide range of different characteristics is seen from this set of maps. First, the chirality that can be readily seen from each cross-section map is evenly distributed among the events: almost half of the flux ropes are right-handed, and the rest are left-handed. Also, they possess various cross-section shapes. A symmetric 2D cross-section of a flux rope would be either circular or elliptical whereas most of them in Figure 8 tend to have significant and irregular elongation in either horizontal, vertical, or other directions. The solutions are completely 2D with nested closed flux surfaces or transverse field line loops of arbitrary shapes, clearly indicative of flux rope configurations. Additionally, the information on scale size is also clear on these plots in terms of spatial extent along the x- or y-axis. For example, the largest one in Figure 7 is about 0.13 au (#25 in Table 1), while the smallest one is near 0.01 au. In general, the axial magnetic field B_z and the transverse magnetic field magnitudes are comparable with each other.

6. Discussion and Conclusion

The connection between magnetic flux ropes and particle acceleration has been established on the basis of prior particle transport theories (Zank et al. 2014, 2015; le Roux et al. 2015, 2016, 2018), which show that multiple interacting magnetic flux ropes can accelerate charged particles through magnetic reconnection-related processes. It has been observed that magnetic reconnection is associated with the energization of ions and electrons in solar flares, the magnetosphere, and solar wind (e.g., Lin et al. 2003; Burch et al. 2016; Khabarova & Zank 2017). The basic acceleration mechanisms include first- and second-order Fermi acceleration by magnetic island contraction and merging, and direct acceleration by reconnection electric field generated by island merging. These mechanisms have been studied using transport theory and simulations (e.g., Drake et al. 2006; Oka et al. 2010; Du et al. 2018). Turbulence can be related to particle acceleration in the sense that flux ropes are representative of quasi-2D turbulence

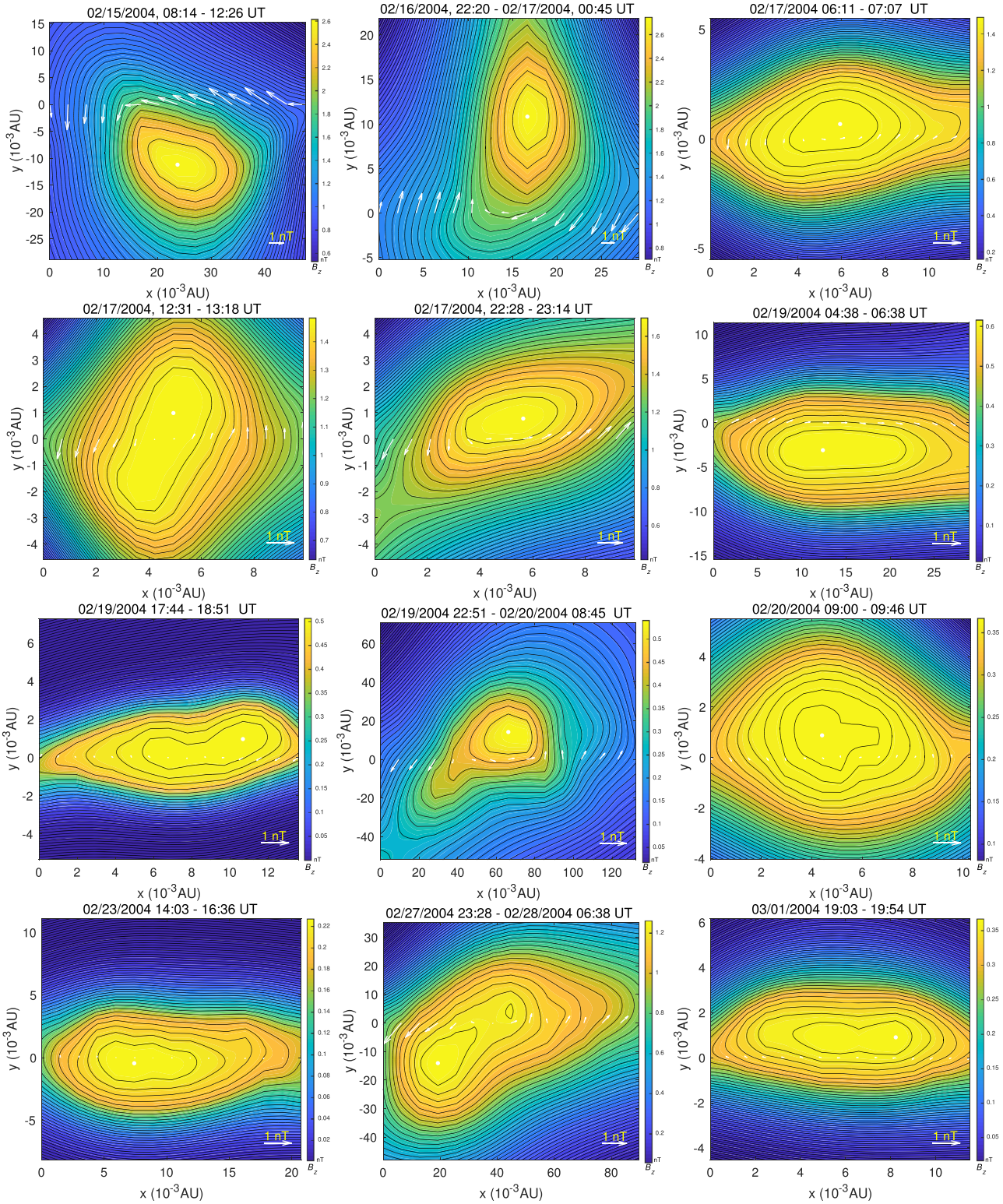

Figure 8. Reconstruction maps of selected small-scale flux ropes. The format is the same as the left panel of Figure 7.

(e.g., Dmitruk et al. 2004; Matthaeus et al. 2007; Greco et al. 2009; Servidio et al. 2009; Zank et al. 2017). The generation of small-scale magnetic flux ropes is intrinsic to MHD turbulence.

In this paper, we present a detailed observational analysis of an unusual energetic particle flux enhancement event reported by Zhao et al. (2018b). We study the period from 2004 February 13 to March 3 using *Ulysses* measurements, discovering the existence and characteristics of small-scale flux ropes via the GS reconstruction approach. Based on our analysis, we find that the unusual particle flux enhancement (around February 14–22) can be associated with small-scale magnetic flux ropes generated in the SIR structure bounded by an FS–RW pair. A typical HCS crossing is identified within the SIR, which may create favorable conditions for generating

small-scale dynamic magnetic islands that are responsible for local particle acceleration. A later FW–RW pair with an embedded large-scale MC is identified during the period around February 25–29. This FW–RW pair has not steepened into shocks. In contrast to the previous SIR structure, only the lower energy particle fluxes are strongly enhanced upstream and at the FW/RW fronts. Our study indicates that the interaction of the HCS with a shock/compressional wave may be a key component in creating the unusual energetic particle flux enhancement within an SIR structure. On the other hand, the presence of a large-scale MC structure may not be conducive to the generation of small-scale magnetic islands in its vicinity, and that the strong MC field may suppress the subsequent energization process and lead to a decrease of energetic particle flux within the MC structure.

The analysis of the energetic particle spectrum shows that the "quiet-time" spectrum does not exhibit a clear PL shape in the considered energy range of ~62 keV–4.4 MeV during the period of interest, as a bump is seen in the lower energy part. A PL energetic particle spectrum is typical in the close vicinity of shocks or strong compressional waves, where low-energy particle fluxes are strongly enhanced. However, the 1D stationary DSA theory fails to predict the PL index of the particle spectrum in this event. Double PL spectra are observed downstream of the FS and HCS, and the lower energy portion is further hardened compared to the spectrum at the shock due to the great enhancement in medium- to high-energy particle fluxes. By contrast, the particle spectrum within the MC is very similar to the "quiet-time" spectrum that shows a bump at the low energies. These features illuminate the different effects of small-scale magnetic flux ropes and large-scale MCs on particle acceleration. We note that subtracting the background spectrum from the acceleration region would result in a slightly harder PL, and possibly a broken PL. However, the background spectrum may not be simply the far upstream "quiet-time" spectrum shown in Figure 3(a). On the other hand, the particle transport theory (Zank et al. 2014) does predict the total spectrum and subtracting the background is not necessary. Based on the above reasons, we do not subtract the "quiet-time" spectrum in this paper. Nevertheless, this may be worth exploring further.

Using a PSD analysis of the magnetic field fluctuations, we show that the magnetic turbulence level is highly enhanced within the FS/FW–RW pairs. Increased wave activity immediately upstream of the second reverse wave is observed and is consistent with previous studies (e.g., Bamert et al. 2004; Zank et al. 2006; Adhikari et al. 2016). The strong downstream turbulence, mostly 2D, may indicate the enhanced generation of small-scale dynamic magnetic islands and thus contribute to the trapping and acceleration of energetic particles (e.g., Zank et al. 2014, 2015; le Roux et al. 2015, 2016, 2018), although the PSD analysis itself cannot provide definite evidence of the flux rope structures.

Using an automatic GS reconstruction technique, we identify 52 magnetic flux ropes during the time period of interest. This provides further evidence of the presence of magnetic flux ropes and thus supports the scenario of local particle acceleration related to magnetic reconnection processes (Zank et al. 2014; Zhao et al. 2018b). Chen et al. (2018) identified ~1100 small-scale flux ropes in the year 2004 using *Ulysses* data, which translates to ~3 per day. We find 18 flux ropes within the ~4 day period of the SIR, which is slightly more than average. This is consistent with previous studies, e.g., Rouillard et al. (2009, 2010), Kilpua et al. (2012), and Yu et al. (2014), who find that SIRs often produce small-scale flux ropes. Note that we use more restrictive detection criteria than Chen et al. (2018), e.g., we have removed flux ropes that have very small sizes (<0.004 au). Thus, the two numbers may not be readily comparable since the average number of flux ropes may have been fewer than ~3 per day in 2004 with more restrictive criteria. On the other hand, both theoretical and observational studies suggest that flux ropes are more likely to be produced near the HCS (Cartwright & Moldwin 2010; Khabarova et al. 2016; Hu et al. 2018; le Roux et al. 2018). The HCS embedded in the SIR may create favorable conditions for generating more flux ropes, and thus provide support for the magnetic island-related local acceleration of particles.

We emphasize again that the acceleration processes require the dynamic interaction of magnetic flux ropes, such as contraction and merging. However, both the PSD analysis and GS reconstruction have the caveat that they can only handle quasistatic turbulence and structures from observations. Therefore, we cannot address questions regarding flux rope compressibility or reconnection rate. The transport and acceleration theories suggest that these dynamic properties are important for acceleration efficiency (e.g., Zank et al. 2014; le Roux et al. 2018). The inclusion of flux rope dynamics in the GS method is still under development. Nevertheless, our analysis provides evidence for the presence of magnetic flux ropes in the acceleration region, which is a necessary condition for flux rope acceleration mechanisms to be effective.

In conclusion, our analysis suggests that the observed unusual energetic particle flux enhancement can be attributed to turbulence and small-scale magnetic islands generated by the interaction of a shock–wave pair and HCS. Such favorable conditions for local particle acceleration mechanisms associated with small-scale magnetic islands may be universal throughout the heliosphere and will be a topic for future studies.

We thank the University of Helsinki for providing the Heliospheric Shock Database (http://ipshocks.fi/database). We acknowledge the partial support of the NSF EPSCoR RII-Track-1 Cooperative Agreement OIA-1655280, NASA grants NNX08AJ33G, Subaward 37102-2, NNX14AC08G, NNX14AJ53G, A99132BT, RR185-447/4944336 and NNX12 AB30G. G.P.Z. is partly supported by the International Space Science Institute (ISSI), both through the award of the 2017 Johannes Geiss Fellowship and in the framework of an International Team Project 405 entitled "Current Sheets, Turbulence, Structures and Particle Acceleration in the Heliosphere." G.P.Z. and S.D. acknowledge partial support by the NSF/DOE Partnership in Basic Plasma Science and Engineering via NSF grant PHY-1707247. Y.C. and Q.H. acknowledge partial support from SAO subcontract SV4-84017 and NASA grants NNX15AI65G and NNX17AB85G.

ORCID iDs

L.-L. Zhao https://orcid.org/0000-0002-4299-0490
G. P. Zank https://orcid.org/0000-0002-4642-6192
Q. Hu https://orcid.org/0000-0002-7570-2301
J. A. le Roux https://orcid.org/0000-0001-9199-2890
S. Du https://orcid.org/0000-0003-1134-3909
L. Adhikari https://orcid.org/0000-0003-1549-5256

References

Adhikari, L., Zank, G. P., Hunana, P., & Hu, Q. 2016, ApJ, 833, 218
Alexandrova, O., Carbone, V., Veltri, P., & Sorriso-Valvo, L. 2008, ApJ, 674, 1153
Ambrosiano, J., Matthaeus, W. H., Goldstein, M. L., & Plante, D. 1988, JGR, 93, 14383
Axford, W. I., Leer, E., & McKenzie, J. F. 1982, A&A, 111, 317
Axford, W. I., Leer, E., & Skadron, G. 1977, ICRC, 11, 132
Bamert, K., Kallenbach, R., Ness, N. F., et al. 2004, ApJL, 601, L99
Bell, A. R. 1978, MNRAS, 182, 147
Bieber, J. W., Wanner, W., & Matthaeus, W. H. 1996, JGR, 101, 2511
Blandford, R. D., & Ostriker, J. P. 1978, ApJL, 221, L29
Burch, J. L., Torbert, R. B., Phan, T. D., et al. 2016, Sci, 352, aaf2939
Burlaga, L., Sittler, E., Mariani, F., & Schwenn, R. 1981, JGR, 86, 6673
Burlaga, L. F., Florinski, V., & Ness, N. F. 2018, ApJ, 854, 20
Cane, H. V., & Lario, D. 2006, SSRv, 123, 45
Cartwright, M. L., & Moldwin, M. B. 2010, JGRA, 115, A08102
Chen, C. H. K. 2016, JPlPh, 82, 6
Chen, Y., Hu, Q., le Roux, J., & Zheng, J. 2018, JPhCS, 1100, 012006
Chian, A. C.-L., & Muñoz, P. R. 2011, ApJL, 733, L34
Dmitruk, P., Matthaeus, W. H., & Seenu, N. 2004, ApJ, 617, 667
Drake, J. F., Swisdak, M., Che, H., & Shay, M. A. 2006, Natur, 443, 553
Du, D., Zuo, P. B., & Zhang, X. X. 2010, SoPh, 262, 171
Du, S., Guo, F., Zank, G. P., Li, X., & Stanier, A. 2018, ApJ, 867, 16
Ebert, R. W., McComas, D. J., Elliott, H. A., Forsyth, R. J., & Gosling, J. T. 2009, JGRA, 114, A01109
Feng, H. Q., Wu, D. J., Lin, C. C., et al. 2008, JGRA, 113, A12105
Forsyth, R. J., & Gosling, J. T. 2001, in The Heliosphere Near Solar Minimum. The Ulysses Perspective, ed. A. Balogh, R. G. Marsden, & E. J. Smith (Berlin: Springer Praxis), 107
Gary, S. P., & Smith, C. W. 2009, JGRA, 114, A12105
Goldstein, M. L., Matthaeus, W. H., & Ambrosiano, J. J. 1986, GeoRL, 13, 205
Gordon, B. E., Lee, M. A., Möbius, E., & Trattner, K. J. 1999, JGR, 104, 28263
Gosling, J. T., McComas, D. J., Skoug, R. M., & Smith, C. W. 2006, GeoRL, 33, L17102
Greco, A., Matthaeus, W. H., Perri, S., et al. 2018, SSRv, 214, 1
Greco, A., Matthaeus, W. H., Servidio, S., Chuychai, P., & Dmitruk, P. 2009, ApJL, 691, L111
Guo, F., Li, H., Daughton, W., & Liu, Y.-H. 2014, PhRvL, 113, 155005
Guo, F., Liu, Y.-H., Daughton, W., & Li, H. 2015, ApJ, 806, 167
Hau, L.-N., & Sonnerup, B. U. Ö 1999, JGR, 104, 6899
Horbury, T. S., & Schmidt, J. M. 1999, SSRv, 89, 61
Hu, Q. 2017, Sci. China Earth Sci., 60, 1466
Hu, Q., Smith, C. W., Ness, N. F., & Skoug, R. M. 2004, JGRA, 109, A03102
Hu, Q., & Sonnerup, B. U. Ö. 2002, JGRA, 107, 1142
Hu, Q., Zank, G. P., Li, G., & Ao, X. 2013, in AIP Conf. Proc. 1539, SOLAR WIND 13: Proceedings of the 13th International Solar Wind Conference (Melville, NY: AIP), 175
Hu, Q., Zheng, J., Chen, Y., le Roux, J., & Zhao, L. 2018, ApJS, 239, 12
Hunana, P., & Zank, G. P. 2010, ApJ, 718, 148
Jian, L. K., Russell, C. T., Luhmann, J. G., Galvin, A. B., & MacNeice, P. J. 2009, SoPh, 259, 345
Kartavykh, Y. Y., Dröge, W., & Gedalin, M. 2016, ApJ, 820, 24
Khabarova, O., Zank, G. P., Li, G., et al. 2015, ApJ, 808, 181
Khabarova, O. V., & Zank, G. P. 2017, ApJ, 843, 4
Khabarova, O. V., Zank, G. P., Li, G., et al. 2016, ApJ, 827, 122
Kilpua, E. K. J., Jian, L. K., Li, Y., Luhmann, J. G., & Russell, C. T. 2012, SoPh, 281, 391
Krymskii, G. F. 1977, DoSSR, 234, 1306
Lanzerotti, L. J., Gold, R. E., Anderson, K. A., et al. 1992, A&AS, 92, 349
Le, A., Karimabadi, H., Egedal, J., Roytershteyn, V., & Daughton, W. 2012, PhPl, 19, 072120
le Roux, J. A., Zank, G. P., & Khabarova, O. V. 2018, ApJ, 864, 158
le Roux, J. A., Zank, G. P., & Ptuskin, V. S. 1999, JGR, 104, 24845
le Roux, J. A., Zank, G. P., Webb, G. M., & Khabarova, O. 2015, ApJ, 801, 112
le Roux, J. A., Zank, G. P., Webb, G. M., & Khabarova, O. V. 2016, ApJ, 827, 47
Leamon, R. J., Smith, C. W., Ness, N. F., Matthaeus, W. H., & Wong, H. K. 1998, JGR, 103, 4775
Li, G., Zank, G. P., & Rice, W. K. M. 2003, JGR, 108, 1082
Lin, R. P., Krucker, S., Hurford, G. J., et al. 2003, ApJL, 595, L69
Lu, Q., Hu, Q., & Zank, G. P. 2009, ApJ, 706, 687
Lu, Q., Wang, H., Huang, K., Wang, R., & Wang, S. 2018, PhPl, 25, 072126
Lu, S., Lu, Q., Huang, C., & Wang, S. 2013, PhPl, 20, 061203
Marhavilas, P. K., Malandraki, O. E., & Anagnostopoulos, G. C. 2015, P&SS, 117, 192
Matthaeus, W. H., Ambrosiano, J. J., & Goldstein, M. L. 1984, PhRvL, 53, 1449
Matthaeus, W. H., Bieber, J. W., Ruffolo, D., Chuychai, P., & Minnie, J. 2007, ApJ, 667, 956
Mostafavi, P., Zank, G. P., & Webb, G. M. 2017, ApJ, 841, 4
Neugebauer, M., Giacalone, J., Chollet, E., & Lario, D. 2006, JGRA, 111, A12107
Oka, M., Phan, T.-D., Krucker, S., Fujimoto, M., & Shinohara, I. 2010, ApJ, 714, 915
Reames, D. V. 1999, SSRv, 90, 413
Reames, D. V. 2013, SSRv, 175, 53
Rice, W. K. M., Zank, G. P., & Li, G. 2003, JGRA, 108, 1369
Richardson, I. G. 2014, SoPh, 289, 3843
Richardson, I. G. 2018, LRSP, 15, 1
Rouillard, A. P., Davies, J. A., Lavraud, B., et al. 2010, JGRA, 115, A04103
Rouillard, A. P., Savani, N. P., Davies, J. A., et al. 2009, SoPh, 256, 307
Salem, C. S., Howes, G. G., Sundkvist, D., et al. 2012, ApJL, 745, L9
Servidio, S., Matthaeus, W. H., Shay, M. A., Cassak, P. A., & Dmitruk, P. 2009, PhRvL, 102, 115003
Servidio, S., Matthaeus, W. H., Shay, M. A., et al. 2010, PhPl, 17, 032315
Sonnerup, B. U. Ö., & Guo, M. 1996, GeoRL, 23, 3679
Sonnerup, B. U. Ö., & Scheible, M. 1998, ISSIR, 1, 185
Tessein, J. A., Matthaeus, W. H., Wan, M., et al. 2013, ApJL, 776, L8
Tessein, J. A., Ruffolo, D., Matthaeus, W. H., & Wan, M. 2016, GeoRL, 43, 3620
Tessein, J. A., Ruffolo, D., Matthaeus, W. H., et al. 2015, ApJ, 812, 68
Trenchi, L., Bruno, R., Telloni, D., et al. 2013, ApJ, 770, 11
Verkhoglyadova, O. P., Zank, G. P., & Li, G. 2015, PhR, 557, 1
Wang, H., Lu, Q., Huang, C., & Wang, S. 2016, ApJ, 821, 84
Wimmer-Schweingruber, R. F., von Steiger, R., & Paerli, R. 1997, JGR, 102, 17407
Yu, W., Farrugia, C. J., Galvin, A. B., et al. 2016, JGRA, 121, 5005
Yu, W., Farrugia, C. J., Lugaz, N., et al. 2014, JGRA, 119, 689
Zank, G. P., Adhikari, L., Hunana, P., et al. 2017, ApJ, 835, 147
Zank, G. P., Hunana, P., Mostafavi, P., et al. 2015, ApJ, 814, 137
Zank, G. P., le Roux, J. A., Webb, G. M., Dosch, A., & Khabarova, O. 2014, ApJ, 797, 28
Zank, G. P., Li, G., Florinski, V., et al. 2006, JGRA, 111, A06108
Zank, G. P., Li, G., & Verkhoglyadova, O. 2007, SSRv, 130, 255
Zank, G. P., & Matthaeus, W. H. 1992, JGR, 97, 17189
Zank, G. P., & Matthaeus, W. H. 1993, PhFl, A5, 257
Zank, G. P., Rice, W. K. M., & Wu, C. C. 2000, JGR, 105, 25079
Zhao, L. L., Adhikari, L., Zank, G. P., Hu, Q., & Feng, X. S. 2017, ApJ, 849, 88
Zhao, L.-L., Adhikari, L., Zank, G. P., Hu, Q., & Feng, X. S. 2018a, ApJ, 856, 94
Zhao, L. L., Zank, G. P., Khabarova, O., et al. 2018b, ApJL, 864, L34
Zheng, J., & Hu, Q. 2018, ApJL, 852, L23